research papers

Preliminary quantitative analysis of myocardial fatty acid metabolism from fluorescent X-ray computed tomography imaging

**Thet-Thet-Lwin,[a] Tohoru Takeda,[a]* Jin Wu,[a] Naoki Sunaguchi,[b]
Takeshi Murakami,[b] Satoshi Mouri,[b] Seita Nasukawa,[b] Qingkai Huo,[b]
Tetsuya Yuasa,[b] Kazuyuki Hyodo[c] and Takao Akatsuka[b]**

[a]Graduate School of Comprehensive Human Sciences, University of Tsukuba, Tsukuba, Ibaraki
305-8575, Japan, [b]Faculty of Engineering, Yamagata University, Yonezawa-shi, Yamagata 992-
8510, Japan, and [c]High Energy Accelerator Research Organization, Tsukuba-shi, Ibaraki 305-0801,
Japan. E-mail: ttakeda@md.tsukuba.ac.jp

Fluorescent X-ray computed tomography (FXCT) using synchrotron radiation reveals the cross-sectional distribution of specific elements in biomedical objects. The aim of this study was to investigate the feasibility of FXCT imaging to assess the myocardial metabolic state quantitatively. Hearts labelled with non-radioactive iodine myocardial fatty acid agent 15-*p*-(iodophenyl)-3-methylpentadecanoic acid (BMIPP) from cardiomyopathic and normal hamsters were imaged. FXCT images were compared with optical microscope images. Myocardial fatty acid metabolism enhanced with BMIPP was clearly depicted by FXCT, which showed an almost homogeneous image for normal and a heterogeneous image for cardiomyopathic hearts. Morphological structures of the heart such as the left ventricle and myocardial wall were also visualized by FXCT. Optical microscopy showed no fibrosis in normal and slight interstitial fibrosis in cardiomyopathic hearts. In the case of cardiomyopathy, the area of significantly reduced BMIPP uptake was 39% in the short axis of the mid-left ventricle in the FXCT image, whereas a slight interstitial fibrosis of around 12% was recognized by optical microscopy for the same slice. This result indicated that reduced BMIPP uptake was caused by the myocardial fatty acid metabolic abnormality, not by the fibrosis in cardiomyopathy. Thus, FXCT images might be used to assess the quantitative metabolic analysis in small animal models of heart diseases.

1. Introduction

The fluorescent X-ray technique in planar mode, a surface scan technique, is a highly sensitive imaging method for detecting very low contents (of the order of picograms) of specific elements (Iida & Gohshi, 1991). Fluorescent X-ray computed tomography (FXCT) has been developed to reveal the cross-sectional distribution of specific elements in bio-medical objects without cutting slices of the sample (Takeda *et al.*, 1996, 1999, 2001, 2002, 2004; Takeda, Momose *et al.*, 2000; Rust & Weigelt, 1998). In studies of phantom and plant (Simionovici *et al.*, 2001) and sediment particles (Vincze *et al.*, 2002), micro-FXCT images were obtained with a spatial resolution of less than 0.01 mm. Our original FXCT system, designed for biomedical study, improved the spatial resolution from 1 mm to 0.025 mm. Compared with recent molecular

imaging techniques such as micro-PET (positron emission tomography) and micro-SPECT (single photon emission computed tomography), FXCT has the advantage of not requiring the use of a radioactive agent limiting easy preparation of the object. In addition, micro-PET and micro-SPECT cannot depict as fine functional images as the auto-radiogram with a spatial resolution of 0.1–0.025 mm for small animals. Also, with autoradiograms, the specimen labelled with radioactive agent is cut into thin slices, and these slices are exposed on an imaging plate or film.

With FXCT using synchrotron radiation, we successfully imaged the myocardial fatty acid metabolism in normal rat (Takeda, Matsushita *et al.*, 2000; Takeda *et al.*, 2002; Takeda, 2005) and cardiomyopathic hamster (Thet-Thet-Lwin *et al.*, 2005) with BMIPP (^{127}I-BMIPP) labelled with non-radioactive iodine, where the BMIPP is a potential tracer for detecting the

fatty acid metabolism in current clinical SPECT imaging (Fujibayashi *et al.*, 1990; Ogata, 1989; Thet-Thet-Lwin *et al.*, 2003). In this study the myocardial fatty acid metabolism in cardiomyopathic hamster and age-matched normal hamster were quantitatively analyzed using FXCT images, and the FXCT images were compared with optical microscope images with Masson's trichrome (MT) stain.

2. Materials and methods

2.1. Fluorescent X-ray computed tomography

The experiment was carried out at the bending-magnet beamline BLNE-5A of the Tristan accumulation ring (6.5 GeV) at the High Energy Accelerator Research Organization, Tsukuba, Japan. The FXCT system consists of a silicon (220) double-crystal monochromator, an X-ray slit system, a scanning table for the target object, a highly purified germanium (HPGe) detector with a parallel collimator, two pin-diode detectors and a computer system (Fig. 1).

The white X-ray beam was monochromated at 37 keV using the silicon double-crystal monochromator. The photon flux in front of the object was approximately 10^8 photons mm^{-2} s^{-1} for a beam current of 40 mA. The incident monochromatic X-ray beam was collimated into a pencil beam with square cross section (0.25 mm × 0.5 mm) using the X-ray slit system. Fluorescent X-rays were detected by the HPGe detector in photon-counting mode. To reduce the amount of Compton radiation captured by the detector, the HPGe detector was positioned perpendicular to the incident monochromatic X-ray beam.

2.2. Experimental phantom

The experiment was performed using a 10 mm-diameter acrylic phantom with 3 mm holes to evaluate the contrast detectability corresponding to iodine concentrations of 200, 100, 50, 25 and 15 µg ml^{-1}. The phantom was imaged by FXCT using the data acquisition parameters summarized in Table 1.
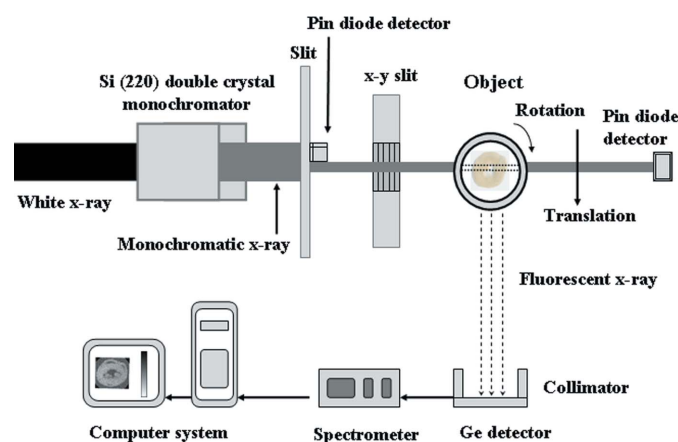

Figure 1
Schematic diagram of the fluorescent X-ray computed tomography system.

Table 1
Summary of the data acquisition parameters.

Slice thickness z line (mm)	Detector–specimen distance (mm)	Translation step over object diameter (mm)	Rotation step over 180°	Exposure time (s)
0.5	80	0.25	3°	7

2.3. Animal preparation and FXCT imaging

A 20 week J2N-k cardiomyopathic hamster and an age-matched J2N-n normal hamster were imaged in this study. Under anesthesia (pentobarbital 40 mg kg^{-1} weight), hearts were extracted after 5 min intravenous injection of ^{127}I-BMIPP (0.08 mg g^{-1} weight). The hearts labelled with BMIPP were fixed by formalin and then imaged by FXCT, placing them in an acrylic cell under the same data acquisition parameters as for the phantom study. Here, five short-axis slices of heart in cardiomyopathy and three short-axis slices in normal hamster were imaged by FXCT.

2.4. Histological staining

After FXCT imaging, specimens were cut into 0.02 mm-thick slices. The degree of fibrosis and its area were evaluated by optical microscopy (Biozero, Keyence Co., Japan) with MT stain, because fibrotic tissue does not uptake BMIPP.

Our experiment was approved by the Medical Committee for the Use of Animals in Research of the University of Tsukuba, and it conformed to the guidelines of the American Physiological Society.

2.5. Image reconstruction

The fluorescent X-ray data were corrected for the attenuation of the incident beam and the emitted fluorescent X-rays within the object. By observing the spectrum of the iodine fluorescent $K\alpha$ line, the distribution of iodine in the object was imaged. FXCT images were reconstructed using an algebraic reconstruction technique which included the attenuation process (Yuasa *et al.*, 1997).

2.6. Image analysis

For quantitative analysis, we measured the fluorescent X-ray intensity of iodine from phantom and myocardium images, and the background intensity was measured outside the area of the target organ, using the image manipulating software NIH *Image* 1.62 (http://rsb.info.nih.gov/nih-image/). Here, the signal-to-noise ratio (SNR) for the region of interest was defined as the average intensity of the region of interest divided by the standard deviation of the background intensity, as calculated by the following equation,

$$SNR = \frac{\text{Average(fluorescent intensity of iodine} - \text{background intensity)}}{\text{standard deviation of background intensity}}.$$

In the FXCT and optical microscope images, each left ventricle was divided into four regions, corresponding to the anterior wall, lateral wall, inferior wall and septum regions, as shown in Fig. 2. The fluorescent X-ray intensity of iodine was measured
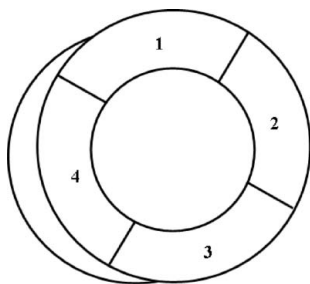
Figure 2
Schematic diagram of standard segmentation for analysis. 1, Anterior wall; 2, lateral wall; 3, inferior wall; 4, septum.
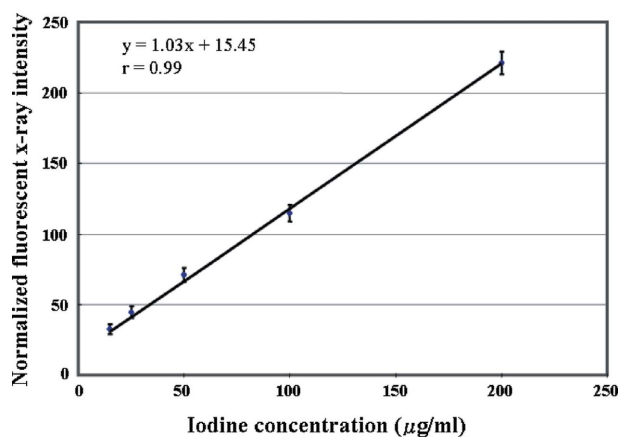

Figure 3
Relationship between fluorescent X-ray intensity and iodine concentration.

Table 2
Mean fluorescent X-ray intensity and SNR for different iodine concentrations.

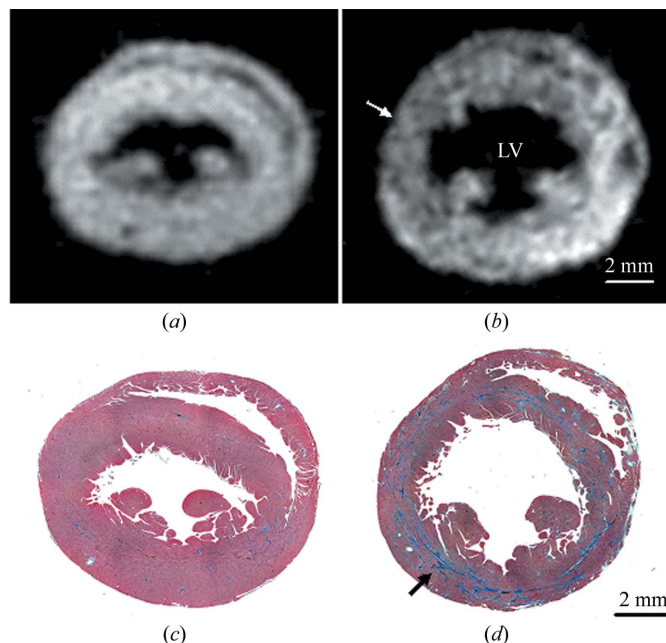|	Iodine concentration ($\mu g\ ml^{-1}$)				
	15	25	50	100	200
Mean fluorescent intensity	29 ± 4	41 ± 4	71 ± 5	115 ± 6	221 ± 8
Signal-to-noise ratio	6.0	8.6	11.9	24.4	51.6

Figure 4
FXCT images of (a) normal myocardium and (b) cardiomyopathic myocardium. Optical microscope pictures with MT stain of (c) normal and (d) cardiomyopathic myocardium. Nearly homogenous BMIPP uptake was observed in normal myocardium. Heterogeneous BMIPP uptake, dilated left ventricle (LV) and mild thinning of the left ventricular wall (white arrow) were observed in cardiomyopathic myocardium. Interstitial fibrosis stained with blue (arrow) was clearly observed in cardiomyopathic myocardium.

for all regions of normal and cardiomyopathic myocardium. The area percentage of fibrosis in each myocardial region was measured from the corresponding optical microscope picture of cardiomyopathic myocardium. All values were expressed as mean ± standard deviation (SD). A p value of less than 0.05 was considered to indicate a statistically significant difference.

3. Results

In the phantom study, good linear correlation was observed between the iodine concentration and the fluorescent X-ray intensity ($r = 0.99$) (Fig. 3). A high SNR was observed for the high iodine-concentration image (Table 2). Myocardial BMIPP uptake was estimated from the result of the linear regression curve of fluorescent X-ray intensity *versus* iodine concentration.

FXCT images revealed that BMIPP was distributed homogeneously in normal myocardium, whereas it was distributed heterogeneously in cardiomyopathic myocardium. In normal hamster, the mean BMIPP uptake value of each slice was not statistically different among the three short-axis images: 177.2 ± 18.5, 180.1 ± 17.9 and 179.1 ± 18.0. In cardiomyopathic hamster, the mean BMIPP uptake value of each slice was also not statistically significant among the five short-axis images: 151.1 ± 26.5, 164.6 ± 25.8, 157.8 ± 23.1, 150.0 ± 24.7 and 149.0 ± 25.6. The mean BMIPP uptake value of each slice in cardiomyopathic hamster heart was lower than

that in normal heart and its standard deviation was larger than that of normal heart.

Short-axis images of the mid-ventricular level in normal and cardiomyopathic hamsters (Figs. 4a and 4b) were analyzed in detail for regions of each slice. In these images the mean BMIPP uptake in normal myocardium was 1.2 times higher than that in cardiomyopathic myocardium ($177.2 \pm 18.5\ \mu g\ ml^{-1}$ *versus* $151.1 \pm 26.5\ \mu g\ ml^{-1}$). The mean value of BMIPP uptake for each myocardial region is shown in Table 3. The statistical difference in the myocardial region was not recognized in normal myocardium; however, the reduced uptake at the septum and inferior wall was observed in cardiomyopathic myocardium. The BMIPP uptake in cardiomyopathic myocardium shifted to a lower value compared with that in normal myocardium (Fig. 5). To assess the myocardial area of the reduced fatty acid metabolism, the lower limit of normal BMIPP uptake was assumed to be $140.2\ \mu g\ ml^{-1}$, *i.e.* the mean BMIPP uptake value ($177.2\ \mu g\ ml^{-1}$) minus 2SD ($37.0\ \mu g\ ml^{-1}$) in normal myocar-

Table 3
Mean BMIPP uptake, and percentile area of reduced BMIPP uptake and fibrosis for each myocardial region of the mid-left ventricle.

State	Left-ventricle regions			
	Anterior wall	Lateral wall	Inferior wall	Septum
Normal (μg ml^{-1})	176.3 ± 13.4	174.3 ± 12.5	179.2 ± 15.2	181.1 ± 14.3
Cardiomyopathy (μg ml^{-1})	167.5 ± 24.1	156.8 ± 22.7	134.5 ± 19.5	147.1 ± 28.2
Uptake $-$ 2SD of normal myocardium (%)	18.3	20.7	75.5	41.3
Percentile fibrosis area (%)	6.9	15.3	11.5	12.3
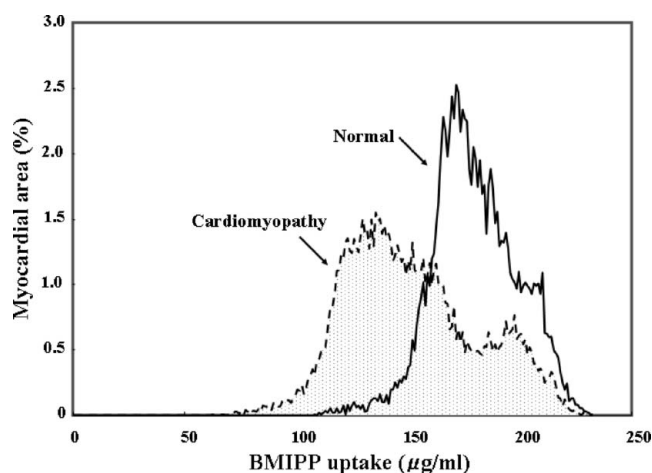
Figure 5
Area distribution of myocardial BMIPP uptake for normal myocardial (full line) and cardiomyopathic myocardium (dotted line). Low BMIPP uptake areas in cardiomyopathic myocardium were increased relative to normal myocardium.

dium. The reduced fatty acid metabolic area was 39.1% of the whole left ventricle in the case of cardiomyopathic myocardium.

In the same slices as used for the FXCT image, optical microscopy with MT stain depicted no fibrosis in normal myocardium and only a slight interstitial fibrosis in cardiomyopathic myocardium (Figs. 4c and 4d). An area of 12.0% was observed as interstitial fibrosis in the whole short-axis slice of the mid-left ventricle. Areas of this interstitial fibrosis partially corresponded to that of reduced BMIPP uptake in the FXCT images (Table 3).

In addition, morphological structures such as papillary muscle, wall thickness and left ventricle diameter were also approximately visualized in the FXCT images. Ventricular dilatation and mild thinning of the myocardial wall were observed in the cardiomyopathic myocardium cases.

4. Discussion

The state of the myocardial fatty acid metabolism corresponding to the BMIPP uptake was clearly depicted by FXCT images with 0.25 mm spatial resolution and 0.5 mm slice thickness. Morphological changes of myocardium such as ventricular dilatation and thinning of myocardial wall were also visualized approximately. The activity of the fatty acid metabolism was decreased heterogeneously in cardiomyopathic myocardium, whereas suitable metabolic activity was observed homogeneously in normal myocardium. These findings were similar to our previous study using autoradiography with radioactive-iodine-labelled BMIPP (^{125}I-BMIPP) (Thet-Thet-Lwin et al., 2004).

Since the fibrotic tissue does not uptake BMIPP, the degree of interstitial fibrosis was evaluated by optical microscopy with MT stain. In the case of cardiomyopathic myocardium, optical microscopy showed slight interstitial fibrosis, i.e. 12% of the mid-left ventricle. The region of interstitial fibrosis partially corresponded to that of reduced BMIPP uptake in the FXCT image of the same object. However, the area of significantly reduced BMIPP uptake (39% of the mid-left ventricle) in the FXCT image was 3.3 times larger than that of the interstitial fibrosis shown in the optical microscope image. This result indicated that reduced BMIPP uptake was caused by a myocardial fatty acid metabolic abnormality rather than by fibrosis for the cardiomyopathic hamster myocardium.

In current biomedical studies, autoradiograms with various radioactive tracers play an important role as fine functional images for biomedical tissue. However, in autoradiograms the use of a radioactive agent limits the easy preparation of the sample, such as various pathological stains, and radiation exposure to researchers is an important problem. Without the use of radioactive agents, our FXCT image could reveal significant fine functions in myocardium similar to autoradiograms.

The FXCT method used in this study is a prototype imaging system, so the image acquisition time was not optimal and long. Now we are developing high-speed FXCT systems to shorten the data acquisition time, by improving the mechanical scanning system and introducing a high-count-rate detector system.

5. Conclusion

Myocardial fatty acid metabolism was evaluated using FXCT images, and quantitative analysis of FXCT images revealed the pathophysiological state both in normal and cardiomyopathic hamster. FXCT with non-radioactive agent has a high spatial resolution, so it might be an alternative to the autoradiogram with radioactive agent for the depiction and quantitative analysis of detailed biomedical functions.

was performed under the auspices of the High Energy Accelerator Research Organization (2003G315, 2005G308).

References

Fujibayashi, Y., Yonekura, Y., Takemura, Y., Wada, K., Matsumoto, K. & Tamaki, N. (1990). *J. Nucl. Med.* **31**, 1818–1822.

Iida, A. & Gohshi, Y. (1991). *Handbook on Synchrotron Radiation*, Vol. 4, edited by S. Ebashi, M. Koch and E. Rubenstein, pp. 307–348. Amsterdam: Elsevier.

Ogata, M. (1989). *Kakuigaku*, **26**, 69–76.

Rust, G. F. & Weigelt, J. (1998). *IEEE Trans. Nucl. Sci.* **45**, 75–88.

Simionovici, A., Chukalina, M., Gunzler, F., Schroer, Ch., Snigirev, A., Snigireva, I., Tummler, J. & Weitkamp, T. (2001). *Nucl. Instrum. Methods*, A**467/468**, 889–892.

Takeda, T. (2005). *Nucl. Instrum. Methods*, A**548**, 38–46.

Takeda, T., Akiba, M., Yuasa, T., Kazam, M., Hoshino, A., Watanabe, Y., Hyodo, K., Dilmanian, F. A., Akatsuka, T. & Itai, Y. (1996). *Proc. SPIE*, **2708**, 685–695.

Takeda, T., Matsushita, S., Wu, J., Yu, Q., Thet-Thet-Lwin, Zenia, T., Yuasa, T., Hyodo, K., Dilmanian, F. A., Akatsuka, T. & Itai, Y. (2000). *Proc. IEEE-EMB*, pp. 276–277.

Takeda, T., Momose, A., Yu, Q., Yuasa, T., Dilmanian, F. A., Akatsuka, T. & Itai, Y. (2000). *Cell. Mol. Biol.* **46**, 1077–1088.

Takeda, T., Tsuchiya, Y., Kuroe, K., Zenia, T., Wu, J., Yu, Q., Thet-Thet-Lwin, Yashiro, T., Yuasa, T., Dilmanian, F. A., Itai, Y. & Akatsuka, T. (2004). *Proceedings of the Eighth International Conference on Synchrotron Radiation Instrumentation (SRI2003), AIP Conference Proceedings 705*, pp. 1320–1323. Melville, NY: American Institute of Physics.

Takeda, T., Yu, Q., Yashiro, T., Zenian, T., Wu, J., Hasegawa, Y., Thet-Thet-Lwin, Hyodo, K., Yuasa, T., Dilmanian, F. A., Akatsuka, T. & Itai, Y. (2001). *Nucl. Instrum. Methods*, A**467/468**, 1318–1321.

Takeda, T., Yu, Q., Yuasa, T., Hasegawa, Y., Yashiro, T., Itai, Y. & Akatsuka, T. (1999). *Proc. SPIE*, **3772**, 258–267.

Takeda, T., Zenia, T., Wu, J., Yu, Q., Thet-Thet-Lwin, Tsuchiya, Y., Rao, D. V., Yuasa, T., Yashiro, T., Dilmanian, F. A., Itai, Y. & Akatsuka, T. (2002). *Proc. SPIE*, **4503**, 299–309.

Thet-Thet-Lwin, Takeda, T., Wu, J., Fumikura, Y., Iida, K., Kawano, S., Yamaguchi, I. & Itai, Y. (2003). *Eur. J. Nucl. Med. Mol. Imaging*, **30**, 966–973.

Thet-Thet-Lwin, Takeda, T., Wu, J., Sunaguchi, N., Tsuchiya, Y., Yuasa, T., Hyodo, K., Dilmanian, F. A., Minami, M. & Akatsuka, T. (2005). *Proceedings of the 6th Asia–Pacific Conference on Medical and Biological Engineering*. PA-3–34:1–4.

Thet-Thet-Lwin, Takeda, T., Wu, J., Tsuchiya, Y. & Itai, Y. (2004). *Ann. Nucl. Med.* **18**, 195–202.

Vincze, L., Vekemans, B., Szaloki, I., Janssens., K, Grieken, R. V., Jones, K. W. & Adams, F. (2002). *Proc. SPIE*, **4503**, 240–248.

Yuasa, T., Akiba, M., Takeda, T., Kazama, M., Hoshino, Y., Watanabe, Y., Huodo, K., Dilmanian, F. A., Aktsuka, T. & Itai, Y. (1997). *IEEE Trans. Nucl. Sci.* **44**, 54–62.